2020

Susceptibility artifact correction for sub-millimeter fMRI using inverse phase encoding registration and T1 weighted regularization

Soan Duong
University of Wollongong, stmd795@uowmail.edu.au

Son Lam Phung
University of Wollongong, phung@uow.edu.au

Abdesselam Bouzerdoum
University of Wollongong, bouzer@uow.edu.au

Harriet Boyd Taylor
University of Wollongong, ht380@uowmail.edu.au

A Puckett

See next page for additional authors

Susceptibility artifact correction for sub-millimeter fMRI using inverse phase encoding registration and T1 weighted regularization

Abstract

© 2020 Elsevier B.V. Background: Functional magnetic resonance imaging (fMRI) enables non-invasive examination of both the structure and the function of the human brain. The prevalence of high spatial-resolution (sub-millimeter) fMRI has triggered new research on the intra-cortex, such as cortical columns and cortical layers. At present, echo-planar imaging (EPI) is used exclusively to acquire fMRI data; however, susceptibility artifacts are unavoidable. These distortions are especially severe in high spatial-resolution images and can lead to misrepresentation of brain function in fMRI experiments. New method: This paper presents a new method for correcting susceptibility artifacts by combining a T1-weighted (T1w) image and inverse phase-encoding (PE) based registration. The latter uses two EPI images acquired using identical sequences but with inverse-PE directions. In the proposed method, the T1w image is used to regularize the registration, and to select the regularization parameters automatically. The motivation is that the T1w image is considered to reflect the anatomical structure of the brain. Results: Our proposed method is evaluated on two sub-millimeter EPI-fMRI datasets, acquired using 3T and 7T scanners. Experiments show that the proposed method provides improved corrections that are well-aligned to the T1w image. Comparison with existing methods: The proposed method provides more robust and sharper corrections and runs faster compared with two other state-of-the-art inverse-PE based correction methods, i.e. HySCO and TOPUP. Conclusions: The proposed correction method used the T1w image as a reference in the inverse-PE registration. Results show its promising performance. Our proposed method is timely, as sub-millimeter fMRI has become increasingly popular.

Disciplines

Engineering | Science and Technology Studies

Publication Details

S. Duong, S. Phung, A. Bouzerdoum, H. Taylor, A. Puckett & M. Schira, "Susceptibility artifact correction for sub-millimeter fMRI using inverse phase encoding registration and T1 weighted regularization," Journal of Neuroscience Methods, vol. 336, 2020.

Authors

Soan Duong, Son Lam Phung, Abdesselam Bouzerdoum, Harriet Boyd Taylor, A Puckett, and Mark M. Schira

Susceptibility Artifact Correction for Sub-millimeter fMRI using Inverse Phase Encoding Registration and T1 Weighted Regularization

S. T. M. Duong[a,*], S. L. Phung[a], A. Bouzerdoum[a,c], H. G. Boyd Taylor[b], A. M. Puckett[d,e], M. M. Schira[b,*]

[a] *School of Electrical, Computer and Telecommunications Engineering, University of Wollongong*
[b] *School of Psychology, University of Wollongong, Australia*
[c] *College of Science and Engineering, Hamad Bin Khalifa University, Qatar*
[d] *School of Psychology, University of Queensland, Australia*
[e] *Queensland Brain Institute, University of Queensland, Australia*

Abstract

Background: Functional Magnetic Resonance Imaging (fMRI) enables non-invasive examination of both the structure and the function of the human brain. The prevalence of high spatial-resolution (sub-millimeter) fMRI has triggered new research on the intra-cortex, such as cortical columns and cortical layers. At present, echo-planar imaging (EPI) is used exclusively to acquire fMRI data; however, susceptibility artifacts are unavoidable. These distortions are especially severe in high spatial-resolution images and can lead to misrepresentation of brain function in fMRI experiments.

New method: This paper presents a new method for correcting susceptibility artifacts by combining a T1-weighted (T_{1w}) image and inverse phase-encoding (PE) based registration. The latter uses two EPI images acquired using identical sequences but with inverse-PE directions. In the proposed method, the T_{1w} image is used to regularize the registration, and to select the regularization parameters automatically. The motivation is that the T_{1w} image is considered to reflect the anatomical structure of the brain.

Results: Our proposed method is evaluated on two sub-millimeter EPI-fMRI datasets, acquired using 3T and 7T scanners. Experiments show that the proposed method provides improved corrections that are well-aligned to the T_{1w} image.

Comparison with existing methods: The proposed method provides more robust and sharper corrections and runs faster compared with two other state-of-the-art inverse-PE based correction methods, *i.e.* HySCO and TOPUP.

Conclusions: The proposed correction method used the T_{1w} image as a reference in the inverse-PE registration. Results show its promising performance. Our proposed method is timely, as sub-millimeter fMRI has become increasingly popular.

Keywords: Susceptibility artifact, echo-planar imaging, sub-millimeter fMRI, inverse phase-encoding, T_{1w} guided regularization.

1. Introduction

Functional Magnetic Resonance Imaging (fMRI) indirectly estimates the changes in cortical activity, typically by measuring the Blood Oxygenation-Level Dependent (BOLD) signal (Ogawa et al., 1990). Functional MRI allows researchers and medical practitioners to non-invasively examine not only the structure but also the function of the human brain, and hence, fMRI has become widely used in clinical and research settings. At present, fMRI images are mostly acquired using the EPI technique because of its fast temporal imaging capability. For example, EPI takes 1 to 3 seconds to scan a volume compared to about 5 minutes for most other MRI techniques. This capability enables EPI to record rapid changes in brain activity.

Despite its speed, EPI is prone to distortions due to local field inhomogeneities, which are caused by the difference in magnetic susceptibility of various imaged tissues (e.g., fat versus blood) (Ludeke et al., 1985; McRobbie et al., 2003). The field inhomogeneities affect the spatial encoding of the signal. Consequently, they degrade the acquired images by geometrical deformations (stretching and compressing) and intensity modulations (Chang and Fitzpatrick, 1992). These distortions are known as susceptibility artifacts (SAs). The SAs are more severe at high field strengths (Ogawa et al., 1990; Polimeni et al., 2018) and in rapid imaging techniques such as EPI (Schmitt,

*Corresponding author
Email addresses: stmd795@uowmail.edu.au (S. T. M. Duong), mschira@uow.edu.au (M. M. Schira)

2015; Ludeke et al., 1985). These artifacts can be easily seen in the interface regions, particularly between the cerebral cortex and non-brain areas (McRobbie et al., 2003). In practice, SAs are most noticeable along the PE direction. Pertinently, they appear reversed in two EPI images acquired using identical sequences but with inverse PE directions[1] (Jezzard and Balaban, 1995; Hutton et al., 2002; Holland et al., 2010).

The SAs disrupt the geometric correspondence between functional and anatomical data. This disruption subsequently leads to misplacements of detected activation patterns in fMRI studies. Currently, correcting SAs in fMRI is often avoided for two main reasons. First, fMRI data have a spatial resolution of 1mm^3 or greater, where SAs are generally not severe enough to cause a significant problem. However, the impact of the SAs is much more significant in high spatial resolution (sub-millimeter) fMRI, which has become widely used. Second, existing SA correction methods tend to blur the corrected images (Polimeni et al., 2018), which contradicts the goal of acquiring a higher spatial image resolution.

This paper aims to correct SAs in EPI-fMRI images, especially those with sub-millimeter resolutions. We propose to integrate a T_{1w} structural image into a state-of-the-art susceptibility artifact correction (SAC) scheme, known as hyper-elastic susceptibility artifact correction (HySCO) (Ruthotto et al., 2012). The motivation is that the T_{1w} image captures relatively well the shape and size of the tissue. It is widely considered a *gold standard* representation of a subject's brain anatomy (Howarth et al., 2006). The T_{1w} image can capture the high contrast between white-matter and gray-matter tissue (Polimeni et al., 2018). Therefore, it is routinely acquired for every subject participating in fMRI studies, and it is readily available. We call the proposed method $\mathbf{T}_{1w}$ guided **I**nverse phase encoding **S**usceptibility **A**rtifact **C**orrection, or TISAC.

The research contributions of this paper can be highlighted as follows. First, a new T_{1w}-based regularization term is introduced to the HySCO objective function to improve the quality of the corrected image with respect to the brain structure captured by the T_{1w} image. Second, the regularization parameters of the registration problem are selected automatically through a Bayesian optimization framework with a Gaussian process prior. Note that choosing the best regularization parameters is a critical step in solving the SAC optimization problem. Furthermore, we evaluate the performance of the proposed method and compare it with existing SAC methods using two high-resolution EPI-fMRI datasets: one with an isotropic resolution of $1 \times 1 \times 1$ mm^3 acquired by a 3 Tesla (T) scanner, and the other with a resolution of $0.833 \times 0.833 \times 0.810$ mm^3 acquired by a 7T scanner.

The remainder of this paper is organized as follows. Section 2 presents the related work and the general mathematical framework of the inverse-PE based correction method. Section 3 introduces our proposed method. Section 4 presents experiments and analysis of the proposed method and the related methods. Finally, Section 5 summarizes our work.

[1] In fMRI, the phase encoding direction is also known as the *polarity of phase-encoding gradient* or the *blip*.

2. Related work

In this section, an overview of the existing SAC methods is presented in Subsection 2.1. The inverse-PE SAC formation is then described in Subsection 2.2. Finally, the HySCO method is discussed in Subsection 2.3.

2.1. Susceptibility artifact correction methods

Several SAC methods have been proposed for multiple types of MRI, such as structural MRI, diffusion-weighted MRI (DWI), and fMRI. In general, they can be divided into four categories: (i) fieldmap based; (ii) point spread function (PSF) based; (iii) image registration based; and (iv) inverse phase-encoding (PE) based methods. Table 1 summarizes the SAC methods discussed below.

Fieldmap based SAC methods estimate phase dispersions caused by the field inhomogeneity. The estimated phase dispersion over the entire scanned view is called the fieldmap. An early approach derives the fieldmap from two complex MRI images acquired by different values of echo time (TE) (Hutton et al., 2002). Another approach requires modified MRI sequences to produce the fieldmap quickly (Wan et al., 1997; Chen and Wyrwicz, 1999; Techavipoo et al., 2008). After the fieldmap is estimated, the corrected images can be obtained by unwarping distorted images (Jezzard and Balaban, 1995; Reber et al., 1998), or rewinding the additional accumulated phase in k-space (Kadah and Hu, 1997), thereby obtaining the corrected image. There have been multiple approaches to estimate the fieldmap. The main limitation of unwarping in the image space is the lack of intensity correction. Rewinding in k-space allows both geometric and intensity corrections but typically requires customized sequences.

Point spread function based SAC methods consider an acquired image as a convolution between the "true" image with a PSF. By estimating the PSF of the system, the undistorted image can be reconstructed. A PSF estimation technique based on constant time imaging was first introduced by Robson et al. (1997) for correcting EPI distortions and quantifying the MRI degradation. Subsequently, the PSF estimation was adopted to correct EPI distortions by Munger et al. (2000); Zeng and Constable (2002). A further optimized PSF estimation was proposed by integrating parallel imaging into the acquisition to correct distortions faster and more reliably, even at high field strengths (Zaitsev et al., 2004). PSF-based SAC methods can correct both geometric distortions and intensity modulations; however, they require the MRI scanner to support configurable MRI sequences.

Image registration based SAC methods map the distorted EPI images to a reference image using a non-rigid

Table 1: Representative methods for correcting SAs (Seq. mod. = pulse sequence modified).

Category	Seq. mod.	Authors	Year	Datatype	Description
Fieldmap	No	Jezzard and Balaban	1995	EPI	Use the fieldmap derived from complex images acquired by different TEs to unwarp the distorted images.
		Reber et al.	1998	EPI	Smooth the displacement derived by the method in Jezzard and Balaban (1995) using a 2D Gaussian kernel to increase the signal-to-noise ratio.
		Hutton et al.	2002	fMRI	Derive the fieldmap from EPI images acquired with different TEs.
	Yes	Kadah and Hu	1997	EPI	Use the fieldmap to rewind the additional accumulated phase in k-space (called SPHERE).
		Wan et al.	1997	EPI	Calculate the fieldmap using a set of reference scans generated by turning off the PE gradient of the EPI pulse sequence.
		Chen and Wyrwicz	1999	EPI	Incorporate a set of fieldmaps by the multi-channel modulation algorithm to obtain corrected images.
		Techavipoo et al.	2008	EPI	Derive the fieldmap from EPI images with modified k-space trajectories.
Point spread function	Yes	Robson et al.	1997	EPI	Measure the PSF by an EPI sequence with added PE gradients, constant time but variable magnitude.
		Munger et al.	2000	EPI	Unwarp the distorted image given the measured PSF by a conjugate gradient algorithm.
		Zeng and Constable	2002	EPI	Correct both the intensity and geometric distortions in EPI images by measured PSF as in Robson et al. (1997).
		Zaitsev et al.	2004	EPI	Measure the PSF by integrating a parallel imaging technique into the acquisition.
Image registration	No	Kybic et al.	2000	EPI	Register distorted EPI images by modelling the displacement with splines and using the SSD similarity measure.
		Studholme et al.	2000	fMRI	Register EPI images using a multimodality non-rigid registration algorithm with log-intensity measure.
		Wu et al.	2006	fMRI	Register distorted images based on Thirion's demons.
		Wu et al.	2008	EPI	Register distorted EPI images to a T_{2w} using mutual information.
Inverse-PE	No	Chang and Fitzpatrick	1992	Structural MRIs	Introduce the theoretical justification of the correction using inverse phase-encoded images; correct each 1D image along the PE direction independently by finding pairs of corresponding points in the given two images.
		Andersson et al.	2003	DWI	Model the displacement as a function of discrete cosine basis functions (called TOPUP).
		Holland et al.	2010	fMRI	Model the inverse-PE SAC as a diffusion registration problem.
		Ruthotto et al.	2012	DWI	Introduce an additional non-linear regularizer into the diffusion regularized problem (called HySCO).
		Irfanoglu et al.	2015	DWI	Incorporate a T_{2w} image into the inverse-PE registration.

model. These methods usually estimate displacements in the image volume so that the unwarped image is morphologically matched to the reference image. These methods have several variants, based on the similarity measure between the EPI and reference images, e.g. the sum of squared differences (SSD) (Kybic et al., 2000), log-intensity metric (Studholme et al., 2000), and mutual information (Wu et al., 2006, 2008). An advantage of this approach is that it does not require additional scans as the fieldmap-based methods do. However, methods in this class typically lack intensity distortion corrections and depend strongly on the constraints and parameters of the registration algorithms.

Inverse phase-encoding based SAC methods utilize two inverse-PE images to estimate the displacement field over the image domain. The corrected images are obtained by unwarping the distorted images by the estimated displacement field. Chang and Fitzpatrick (1992) initially introduced the theoretical justification of correcting the SAs using inverse-PE structural images. They then proposed a "cumulative line-integral" method to find the corresponding points, which are used to determine the displacement in two corresponding lines along the PE direction of the given inverse-PE images. Bowtell et al. (1994) implemented the original inverse-PE method for 2D EPI. The corrections of the method proposed by Chang and

Fitzpatrick (1992) are not smooth since the method estimates the displacement in each line along the PE direction independently, without considering surrounding lines. To estimate the displacement field, Andersson et al. (2003) proposed an alternative approach by considering the displacement at a pixel as a function of discrete cosine basis functions to construct an objective function; this method is called TOPUP and is integrated into the FSL package[2]. Holland et al. (2010) integrated the inverse-PE approach into a registration framework to correct SAs. Ruthotto et al. (2012, 2013) combined the registration framework and a constraint inspired by the hyper-elastic image registration to achieve more realistic corrections; this method is called HySCO, and its implementation is included in the SPM12 toolbox[3]. Another approach combines an independent image, specifically a T_{2w} image, into the inverse-PE registration to regularize corrections (Irfanoglu et al., 2015). Inverse-PE based SAC methods can correct both geometric and intensity distortion. They outperform fieldmap and image registration based methods in terms of geometrical correction fidelity, as shown in (Hong et al., 2015). The inverse-PE based approach is the most common SAC method, e.g. being used to correct the fMRI data in the biggest MRI neuroimaging dataset - the Human Connectome Project (HCP) (Essen et al., 2012). However, compared to other SAC approaches, registering corrected images from two inverse-PE images requires many constraints, such as the smoothness of the displacement field and the alignment of the correction to the structural image. The inverse-PE methods may produce less meaningful and blurred corrections if unsuitable constraints are used.

In summary, the existing methods have been designed mostly for DWI images but rarely for fMRI. These methods either require a long scanning time or correct only spatial distortions. Furthermore, they are often inadequate at correcting SAs in high-resolution fMRI, where the distortions are more severe than in low-resolution images.

2.2. Distortion model in the presence of the field inhomogeneity

Let E be the 3D ideal image, and I be an acquired (distorted) image. As shown in (Chang and Fitzpatrick, 1992; Studholme et al., 2000; Holland et al., 2010), the distortion in the presence of field inhomogeneity B in the image domain is modeled as

$$E = I(\mathbf{T})\,|\mathbf{J_T}|, \tag{1}$$

where $\mathbf{T}$ is the non-rigid transformation operator of coordinates from image E to image I, and $\mathbf{J_T}$ is the Jacobian matrix of the transformation $\mathbf{T}$. As shown in (Holland et al., 2010; Ruthotto et al., 2012), the transformation $\mathbf{T}$ at any 3D point $\mathbf{p}$ in E can be written as $\mathbf{T}\colon\ \mathbf{p} \mapsto \mathbf{p} + B(\mathbf{p})\,\mathbf{v}$, where $\mathbf{v}$ denotes the known distortion direction (*i.e.* the PE direction). In practice, the applied PE gradient is considered to be along the first dimension, hence $\mathbf{v} = (1, 0, 0)$. Let $\partial_{\mathbf{v}}(B(\mathbf{p}))$ denote the directional derivative of field B at point $\mathbf{p}$ along the direction $\mathbf{v}$. The Jacobian matrix of the transformation $\mathbf{T}$ at point $\mathbf{p}$ is

$$\mathbf{J}_{\mathbf{T}(\mathbf{p})} = \frac{\partial(\mathbf{p} + B(\mathbf{p})\mathbf{v})}{\partial \mathbf{p}} = \begin{bmatrix} 1 + \partial_{\mathbf{v}}(B(\mathbf{p})) & 0 & 0 \\ 0 & 1 & 0 \\ 0 & 0 & 1 \end{bmatrix}. \tag{2}$$

The distortion model in Eq. (1) can be rewritten as

$$E(\mathbf{p}) = I(\mathbf{p} + B(\mathbf{p})\mathbf{v})\,\big[1 + \partial_{\mathbf{v}}(B(\mathbf{p}))\big]. \tag{3}$$

Here, the term $\big[1 + \partial_{\mathbf{v}}(B(\mathbf{p}))\big]$ denotes the intensity modulation. The term $\mathbf{p} + B(\mathbf{p})\mathbf{v}$ denotes the geometric displacement of the acquired image. In other words, point $\mathbf{p}$ in ideal image E is shifted to point $\mathbf{p} + B(\mathbf{p})\mathbf{v}$ in acquired image I. Since B causes the voxel shifting in the acquired image, B is called the *displacement field*, and $\mathbf{p} + B(\mathbf{p})\mathbf{v}$ is known as the deformation at point $\mathbf{p}$. Fig. 1 illustrates the distortions caused by the displacement field. The ideal image in Fig. 1(a) under the displacement field in Fig. 1(b) is distorted, as shown in Fig. 1(c). It is worth noting that we work with 3D images; however, for simplicity, 2D images are presented throughout this paper.

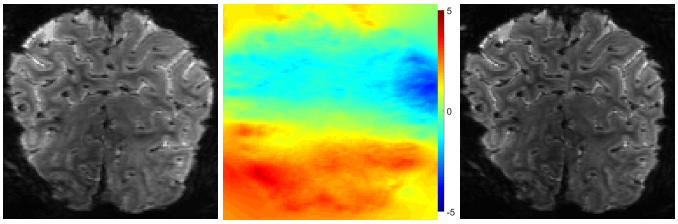

(a) Ideal slice (b) Displacement field (c) Distorted slice

Figure 1: A 2D illustration of the susceptibility-induced distortions. The displacement field is along the PE (horizontal) direction and is expressed in terms of the number of voxels shifted.

Let I_1 and I_2 be two images of a subject in the same brain region, acquired using an identical sequence but with opposite blips. Let B be the field inhomogeneity, and $\mathbf{v}$ be the PE direction for image I_1. The field inhomogeneity and the PE direction for image I_2 are B and $-\mathbf{v}$, respectively. By applying the model in Eq. (3), the corrected images E_1 and E_2 can be described as

$$\begin{cases} E_1(\mathbf{p}) = I_1(\mathbf{p} + B(\mathbf{p})\mathbf{v})\,[1 + \partial_{\mathbf{v}}(B(\mathbf{p}))], \\ E_2(\mathbf{p}) = I_2(\mathbf{p} - B(\mathbf{p})\mathbf{v})\,[1 - \partial_{\mathbf{v}}(B(\mathbf{p}))]. \end{cases} \tag{4}$$

For notational simplicity, hereinafter $X_{\mathbf{p}}$ will refer to the intensity of image X at location $\mathbf{p}$.

2.3. Hyper-elastic susceptibility artifact correction

Recall that the inverse-PE approach estimates the displacement field B based on two images I_1 and I_2 acquired

[2] https://fsl.fmrib.ox.ac.uk/fsl/fslwiki/topup
[3] http://www.diffusiontools.com/documentation/hysco.html

using an identical sequence but with opposite blips. Field B is estimated such that two corrected images E_1 and E_2 are as similar as possible. The estimated B is then used to unwarp the distorted images I_1 and I_2 based on Eq. (4).

The hyper-elastic susceptibility artifact correction method proposed by Ruthotto *et al.* (Ruthotto et al., 2012) uses the inverse-PE approach to correct SAs. To estimate B, Ruthotto *et al.* minimized the SSD-based dissimilarity between unwarped images E_1 and E_2 (Holland et al., 2010; Ruthotto et al., 2012):

$$D(I_1, I_2, B) = D(E_1, E_2) = \frac{1}{2}\int_\Omega (E_{1\mathbf{p}} - E_{2\mathbf{p}})^2 \, d\mathbf{p}. \quad (5)$$

Finding B by minimizing the distance function $D(I_1, I_2, B)$ is categorized as an ill-posed problem (Holland et al., 2010; Ruthotto et al., 2012). Thus, prior knowledge about the smoothness of the displacement field and invertibility of the geometrical transformation was used to regularize B (Ruthotto et al., 2012). To enforce the smoothness of the displacement field, a Tikhonov ($\mathcal{L}_2$) regularizer S^{diff} was integrated into the objective function (Holland et al., 2010):

$$S^{\text{diff}}(B) = \int_\Omega \| \nabla B_{\mathbf{p}} \|^2 \, d\mathbf{p}. \quad (6)$$

To satisfy the invertibility of the transformation, the Jacobian matrix of the geometric transformation in Eq. (4) must be invertible. In other words, Jacobian determinants must be positive for all $\mathbf{p} \in \Omega$. Chang and Fitzpatrick (1992) demonstrated that this constraint could be expressed as $-1 \leqslant \partial_{\mathbf{v}}(B_{\mathbf{p}}) \leqslant 1$, for all $\mathbf{p} \in \Omega$.

Ruthotto et al. (2012), inspired by the control of volumetric change in hyper-elasticity (Burger et al., 2013), introduced an additional non-linear term S^{hyper} to the objective function:

$$S^{\text{hyper}}(B) = \int_\Omega \phi(\partial_{\mathbf{v}}(B_{\mathbf{p}}))\, d\mathbf{p}, \quad \text{with } \phi(z) = \frac{z^4}{1-z^2}. \quad (7)$$

Collectively, Ruthotto et al. (2012) proposed the objective function:

$$\begin{aligned} J(B) = & D(I_1, I_2, B) + \alpha S^{\text{diff}}(B) + \beta S^{\text{hyper}}(B), \\ & \text{s.t.} \quad | \, \partial_{\mathbf{v}}(B_{\mathbf{p}}) \, | \leqslant 1. \end{aligned} \quad (8)$$

The positive and user-defined regularization parameters α and β represent the trade-off between the smoothness and the elasticity of the displacement field B.

The HySCO method estimates B by minimizing the objective function $J(B)$ in Eq. (8), then generates the output (corrected) images using Eq. (4). HySCO can provide output images with high similarity; however, these images are blurry, and they may not align well with the actual brain structure. For example, Fig. 2(a) shows the estimated deformation grid[4] by HySCO, and Fig. 2(b) shows the output image. The output image contains blur trails (e.g. areas denoted by the red arrows), which are caused by over-deformation in the estimated field B. This over-deformation could be reduced by imposing an independent constraint related to the brain structure.

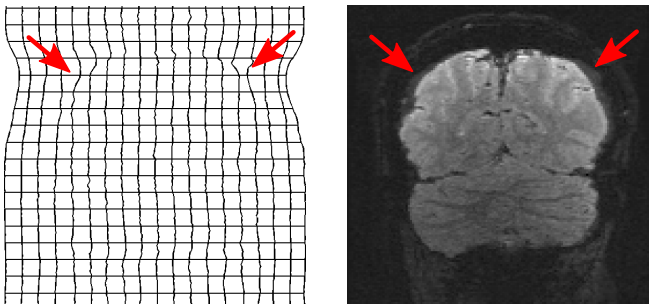

(a) Estimated deformation grid (b) HySCO correction

Figure 2: An example of HySCO results with additional artifacts (red arrows) on the top of the brain.

3. T_{1w}-guided inverse-PE SAC

The T_{1w} structural image, acquired using MPRAGE sequence (Mugler III and Brookeman, 1990) or MP2RAGE (Marques et al., 2010) sequence, is widely considered to reflect the anatomical structure of the brain, especially in the fMRI study (Howarth et al., 2006). In this paper, we propose to incorporate the T_{1w} image to guide the susceptibility artifact correction of high spatial resolution EPI-fMRI images. In the proposed approach, the T_{1w} image is used for two purposes: (i) introducing an additional regularization term for the new objective function, and (ii) selecting the three regularization parameters of the objective function.

3.1. TISAC registration

The inverse-PE correction problem integrated with a T_{1w} structural image can be formulated as finding the displacement field B such that the corrected (unwarped) images E_1 and E_2 satisfy two criteria: (i) be as similar to each other as possible, and (ii) align well with the structural information provided by the T_{1w} image. Ruthotto et al. (2012) proposed the objective function in Eq. (8), which satisfies the first criterion. We introduce a T_{1w}-guided regularization term to address the second criterion. More precisely, the regularization term measures the dissimilarity between the multi-modal images, *i.e.* T_{1w} and EPI-fMRI. Conceptually, minimizing the proposed objective function is equivalent to minimizing the dissimilarity between the corrected EPI-fMRI images and the dissimilarity between corrected images and the T_{1w} image. This subsection is designed to provide an accessible mathematical description of the proposed method.

The proposed regularization term is based on the normalized gradient field, which has been proven to be well-suited for the multi-modal registration problem (Haber

[4]The deformation grid is the sum of the regular grid and the displacement field.

and Modersitzki, 2007). The NGF measure, at any point in an image, reveals the intensity change and its direction. Let $\nabla X_{\mathbf{p}}$ be the gradient at point $\mathbf{p}$ of image X, and ε be a user-defined parameter. As shown in (Haber and Modersitzki, 2007), the NGF measure at point $\mathbf{p}$ is defined as

$$\tilde{\nabla} X_{\mathbf{p}} = \frac{\nabla X_{\mathbf{p}}}{\sqrt{\|\nabla X_{\mathbf{p}}\|^2 + \varepsilon^2}}. \tag{9}$$

The difference between two images X and Y can be measured using the angles formed by NGF vectors at all points in the image domain. Accordingly, the NGF-based distance between two images X and Y is defined as

$$D^{\mathrm{NGF}}(X,Y) = \frac{1}{2}\int_{\Omega} 1 - \langle \tilde{\nabla} X_{\mathbf{p}}, \tilde{\nabla} Y_{\mathbf{p}} \rangle^2 \, d\mathbf{p}, \tag{10}$$

where $\langle \cdot, \cdot \rangle$ denotes the dot-product operator. The value of $D^{\mathrm{NGF}}(X,Y)$ is positive. The smaller the value of $D^{\mathrm{NGF}}(X,Y)$ is, the more similar are the two images.

Let A denote the T_{1w} image. We introduce the T_{1w}-guided regularization term as the sum of the NGF-based distances of image A to each unwarped image of I_1 and I_2 under the displacement field B

$$\begin{aligned} D_A(I_1, I_2, B, A) &= D^{\mathrm{NGF}}(A, E_1) + D^{\mathrm{NGF}}(A, E_2) \\ &= \frac{1}{2}\int_{\Omega} \left[1 - \langle \tilde{\nabla} A_{\mathbf{p}}, \tilde{\nabla} E_{1\mathbf{p}} \rangle^2\right] + \\ &\qquad \left[1 - \langle \tilde{\nabla} A_{\mathbf{p}}, \tilde{\nabla} E_{2\mathbf{p}} \rangle^2\right] d\mathbf{p}. \end{aligned} \tag{11}$$

To summarize, we introduce a new objective function:

$$\begin{aligned} J(B) = {} & D(I_1, I_2, B) + \alpha S^{\mathrm{diff}}(B) + \beta S^{\mathrm{hyper}}(B) + \\ & \gamma D_A(I_1, I_2, B, A) \\ & \text{s.t.} \quad |\, \partial_{\mathbf{v}}(B_{\mathbf{p}}) \,| \leqslant 1 \quad \text{for all } \mathbf{p} \in \Omega. \end{aligned} \tag{12}$$

The displacement field is found by minimizing $J(B)$ in Eq. (12). The positive and user-defined regularization parameters α, β, and γ represent the trade-off between the similarity of the corrected images, the smoothness of B, the elasticity of the displacement, and the similarity to the T_{1w} image of corrected images.

In this paper, the Gauss-Newton method is used for minimization. This method starts with an initial guess of B, e.g. $B^{(0)} \equiv \mathbf{0}$. The next estimate of B is computed iteratively as

$$B^{(k+1)} = B^{(k)} - \lambda^{(k)} \, G^{(k)} \, (H^{(k)})^{-1}, \quad \lambda^{(k)} > 0, \tag{13}$$

where superscript k is the iteration number, $\lambda^{(k)}$ is the learning rate, and $G^{(k)}$ and $H^{(k)}$ are the approximate gradient and Hessian of the objective function J, respectively.

A small learning rate leads to slow convergence, while a large one may lead to invalid $B^{(k+1)}$. Therefore, to select a suitable learning rate, we find the maximum $\lambda^{(k)}$ that produces $B^{(k+1)}$ meeting the constraint in (12) (Nocedal and Wright, 1999). This is done by applying the backtracking line search (Armijo, 1966).

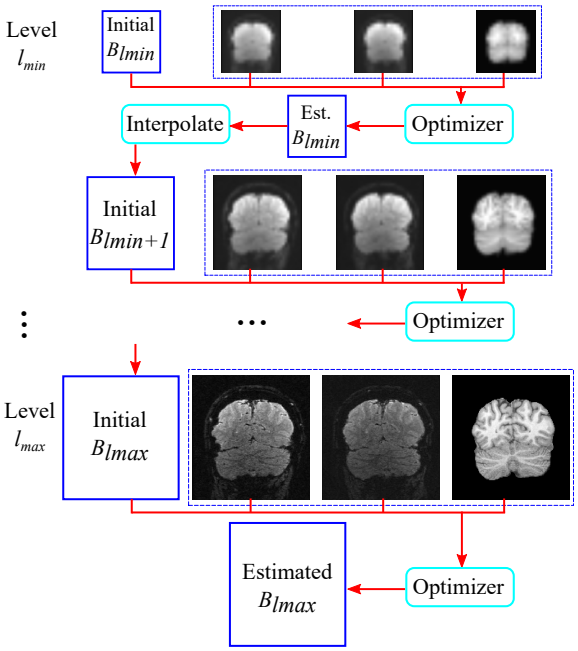

Figure 3: The block diagram of the coarse-to-fine optimization scheme. The displacement field is estimated at each level of data representation.

To avoid local minima and to accelerate the convergence, the Gauss-Newton method is integrated with the coarse-to-fine approach (see Fig. 3). This approach first represents images with multiple resolution levels. The image representation at a coarser level is obtained simply by averaging over adjacent cells. Next, the displacement field in the coarsest level is estimated by minimizing the objective function in (12) using the image representation at this level. The estimated displacement field at the coarser level is interpolated. The interpolated result is considered the initial guess for the optimizer at a finer level. The process of interpolation and estimation is repeated until the displacement field at the finest level is obtained. Finally, the corrected images are obtained by unwarping the distorted images with the estimated field B, as shown in Eq. (4). This coarse-to-fine optimization approach is summarized in Algorithm 1.

3.2. Optimization of hyper-parameters

In the inverse-PE SAC, the choice of the regularization parameters (hyper-parameters) is crucial. Here, we propose a method to select the most suitable regularization parameters for the SAC problem. The proposed hyper-parameters optimization method is based on the Bayesian optimization (BO) with a Gaussian process (GP) prior.

The hyper-parameter optimization is performed by minimizing an error function $f(\mathbf{x})$ of the given SAC method over a dataset D, where $\mathbf{x}$ is a vector of hyper-parameters. The error function here is defined by the sum of the dissimilarity measure M between the T_{1w} image and the corrected fMRI images for the dataset D. In this study, the

Algorithm 1 Coarse-to-fine Gauss-Newton for SAC

Input: I_1, I_2: inverse-PE EPI-fMRI images,
A: T_{1w} image corresponding to fMRI images,
$l_{\min}$, $l_{\max}$: min, max level of data representation.
Output: Corrected images E_1 and E_2.

Derive the multilevel image representation;
$B_{l_{\min}-1} \leftarrow \mathbf{0}$;
for $l = l_{\min} : l_{\max}$ **do**
  Interpolate $B_l^{(0)}$ from B_{l-1}: $B_l^{(0)} \leftarrow \textbf{inter}\,(B_{l-1})$;
  $k \leftarrow 0$;
  Compute the objective function as in Eq. (12):
  $[J, G^{(k)}, H^{(k)}] \leftarrow \textbf{obj\_fnct}\,(I_1, I_2, B_l^{(k)}, A, l)$;
  while not converged **do**
    Compute the new B via backtracking line search:
    $B_l^{(k+1)} \leftarrow \textbf{backtrack\_search}\,(B_l^{(k)}, G^{(k)}, H^{(k)})$;
    Increment k: $k \leftarrow k + 1$;
    Compute the objective function as in Eq. (12):
    $[J, G^{(k)}, H^{(k)}] \leftarrow \textbf{obj\_fnct}\,(I_1, I_2, B_l^{(k)}, A, l)$;
  end while
  $B_l \leftarrow B_l^{(k)}$;
end for
Unwarp I_1 and I_2 using Eq. (4)
  $E_1 \leftarrow \textbf{unwarp}\,(I_1, B_{l_{\max}})$;
  $E_2 \leftarrow \textbf{unwarp}\,(I_2, B_{l_{\max}})$;

MIND-based measure is used (refer to Appendix A for a description of the MIND measure). The mathematical equation of the loss function is:

$$\begin{aligned} f(\mathbf{x}) &= L(\mathcal{S}_{\mathbf{x}}, \mathrm{D}) \\ &= \frac{1}{|\mathrm{D}|} \sum_{I_{1i}, I_{2i}; A_i \in \mathrm{D}} M(\mathcal{S}_{\mathbf{x}}(I_{1i}, I_{2i}),\, A_i) \\ &= \frac{1}{|\mathrm{D}|} \sum_{I_{1i}, I_{2i}, A_i \in \mathrm{D}} M(E_{1i}^{\mathcal{S}_{\mathbf{x}}},\, A_i) + M(E_{2i}^{\mathcal{S}_{\mathbf{x}}},\, A_i), \end{aligned} \tag{14}$$

where $\mathcal{S}_{\mathbf{x}}(I_{1i}, I_{2i})$ represents the corrected images $E_{1i}^{\mathcal{S}_{\mathbf{x}}}$ and $E_{2i}^{\mathcal{S}_{\mathbf{x}}}$ for the inputs I_{1i} and I_{2i}, by applying the SAC method $\mathcal{S}$ with hyper-parameters $\mathbf{x}$. We select the hyper-parameters which give minimum error function. In other words, finding the hyper-parameters is to minimize the error function Eq. (14). Since the error function of the hyper-parameters is computationally expensive, and its distribution is unknown, the hyper-parameter optimization problem is challenging.

BO is a powerful technique for finding extrema of an objective function that has no closed-form expression or is computationally intensive to evaluate (Brochu et al., 2010; Bergstra et al., 2011; Snoek et al., 2012). The BO algorithm uses previous observations, which are pairs of $\{\mathbf{x}, f(\mathbf{x})\}$, to determine what is the next optimal point for sampling the error function.

To be specific, the BO algorithm first computes the posterior expectation of what the function f looks like based on its previous observations. This step is done by first considering that the distribution of $f(\mathbf{x})$ is a normal likelihood with noise. The error function f then can be considered a Gaussian process, which is specified by the mean $\boldsymbol{\mu}$ and covariance $\boldsymbol{\sigma}$ of a normal distribution over possible values of $f(\mathbf{x})$. The means and covariances allow us to update our belief of what the function f looks like. They can be obtained by fitting the GP to a given set of observations $\mathcal{H} = \{(\mathbf{x}_1, f(\mathbf{x}_1)), (\mathbf{x}_2, f(\mathbf{x}_2)), \ldots, (\mathbf{x}_n, f(\mathbf{x}_n))\}$.

Next, a new point is selected to sample the function f so that it provides a higher value of f or is in the unexplored region. As shown in Bergstra et al. (2011), the point can be found by maximizing the expected improvement function, which is defined as

$$\Psi(\mathbf{x}) = \begin{cases} [\mu(\mathbf{x}) - f(\mathbf{x}^*)]\,\Phi(z) + \sigma(\mathbf{x})\,\phi(z) & \text{if } \sigma(\mathbf{x}) > 0 \\ 0 & \text{if } \sigma(\mathbf{x}) = 0 \end{cases}. \tag{15}$$

where $\mathbf{x}^*$ is the current optimal hyper-parameter point, $\mu(\mathbf{x})$ and $\sigma(\mathbf{x})$ are the estimated mean and variance of function f at $\mathbf{x}$ in the previous step, $z = \frac{\mu(\mathbf{x}) - f(\mathbf{x}^*)}{\sigma(\mathbf{x})}$, $\Phi(z)$ is the cumulative distribution, and $\phi(z)$ is probability density function of the standard normal distribution.

Algorithm 2 Hyper-parameters optimization algorithm.

Input: D: dataset.
Output: $\mathbf{x}^*$: optimal hyper-parameters.

$\mathcal{H} \leftarrow \emptyset$;
while not converged **do**
  Fit GP on the observation set: $\{\boldsymbol{\mu}, \boldsymbol{\sigma}\} \leftarrow \mathrm{GP}(\mathcal{H})$;
  Choose the next point for sampling:
  $\hat{\mathbf{x}} \leftarrow \underset{\mathbf{x}}{\operatorname{argmax}}\, \Psi(\mathbf{x} \,|\, \boldsymbol{\mu}, \boldsymbol{\sigma})$;
  Compute the error function at $\hat{\mathbf{x}}$: $f(\hat{\mathbf{x}}) \leftarrow L(\mathcal{S}_{\hat{\mathbf{x}}}, \mathrm{D})$;
  Update the observation set: $\mathcal{H} \leftarrow \mathcal{H} \cup (\hat{\mathbf{x}}, f(\hat{\mathbf{x}}))$;
  Increment k: $k \leftarrow k + 1$;
end while
$\mathbf{x}^* \leftarrow \underset{\mathbf{x} \in \mathcal{H}}{\operatorname{argmin}} f(\mathbf{x})$

The new point obtained by maximizing the expected improvement function $\Psi(\mathbf{x})$ is admitted to the observation set. The procedure of fitting GP and finding the sampling point is repeated until the convergence criterion is met. Algorithm 2 shows the Bayesian optimization for automatically selecting the hyper-parameters.

4. Experiments and results

This section presents the experiments and analysis of the proposed method. Subsection 4.1 describes data acquisition and preprocessing, and Subsection 4.2 presents the evaluation measures. Subsection 4.3 shows the experimental methods, and Subsection 4.4 presents an analysis of the proposed method. Subsection 4.5 shows the comparison of SAC methods, finally Subsection 4.6 discusses the experimental results.

Table 2: A summary of the datasets used in the experiments.

Datasets	No. subjs.	Gender dist.	Age avg.	Volume size	Resolution (mm^3)	Acquisition sequence	Field strength
3T	3	1 female, 2 males	23.67	$192 \times 144 \times 36$	$1 \times 1 \times 1$	2D single-shot GRE-EPI	3T
7T	3	3 males	35.33	$192 \times 192 \times 48$	$0.833 \times 0.833 \times 0.810$	3D GRE-EPI (WIP1080)	7T

4.1. Data acquisition and preprocessing

Two EPI-fMRI datasets of the occipital cortex were used to evaluate the performance of SAC methods. The first dataset had three subjects and was acquired using a 3T scanner with an isotropic resolution of $1 \times 1 \times 1$ mm^3. The second dataset had three subjects and was acquired using a 7T scanner with a resolution of $0.833 \times 0.833 \times 0.810$ mm^3. A brief summary of these datasets is presented in Table 2. The datasets were acquired with the written informed consent from all participating subjects, in accordance to the Human Ethics Committees requirements at the University of Queensland, and the Australian National Health and Medical Research Council's guidelines.

The 3T dataset from three healthy subjects was acquired using a Siemens 3T MAGNETOM PRISMA with a 64-channel head coil and a 2D single-shot gradient-echo (GRE) EPI sequence. Ascending and interleaved coronal slices were acquired with a repetition time (TR) of 3000 milliseconds (ms), which is also the volume repetition time, TE of 30 ms, a flip angle of 90 degrees, and an image size of $192 \times 144 \times 36$. The field of view (FOV) was 144 mm $\times$ 192 mm.

The 7T dataset from three healthy subjects was acquired using a Siemens 7T MAGNETOM whole-body research scanner with a 32-channel head coil (Nova Medical, Wilmington, US) and a 3D EPI sequence WIP1080 (Poser et al., 2010) (Poser et al., 2010). The sequence used a blipped CAIPIRINHA (Breuer et al., 2006; Setsompop et al., 2011), implementation (Poser et al., 2013) with the following parameters: TE of 30 ms, TR of 83 ms, volume repetition of 1992 ms, flip angle of 17 degrees, echo spacing of 1 ms, FOV of 160 mm $\times$ 160 mm, matrix size of $192 \times 192 \times 48$. The image acquisition was accelerated by a factor of 2 in-plane and by a factor of 2 in the slice-encoding direction with a CAIPI-shift of 1. This results in a total acceleration factor of 4. The image reconstruction was done by using the GRAPPA pipeline (Griswold et al., 2002), as provided by the vendor.

Figure 4 shows the three different orientation views (coronal, sagittal, and axial) of 7T inverse-PE EPI images (pink) overlaying on the T_{1w} image (green). The figure demonstrates that the misalignment of EPI to the T_{1w} image occurs mainly in one spatial direction (left-to-right).

Functional MRI data were acquired while subjects were presented with retinotopic mapping stimuli. In the 3T dataset, stimuli consisted of drifting bars, expanding rings, rotating bowties, and flashing full-field (see Fig. 5). Each subject took part in two scanning sessions; in each session, subjects viewed visual stimuli while scanning using either

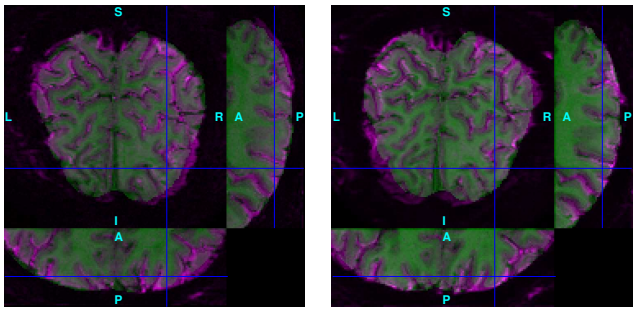

(a) Forward PE EPI image (b) Inverse PE EPI image

Figure 4: Distorted EPI slices overlaying on a T_{1w} image with three different orientation views. The blue lines (cross-hairs) indicate the intersection point of the three views. See the electronic color images.

left-to-right (LR) or right-to-left (RL) blips, such that each blip accounted for half the scans. This resulted in pairs of scans with reversed patterns of distortions in the PE direction. In the 7T dataset, only the rotating bowtie stimulus was used. In each subject, two scans (with 183 or 187 volumes each) were collected with LR blip, and two short 20 s measurements with ten repeated EPI volumes were collected with the inverse blip, one at the beginning of the experimental runs and one at the end.

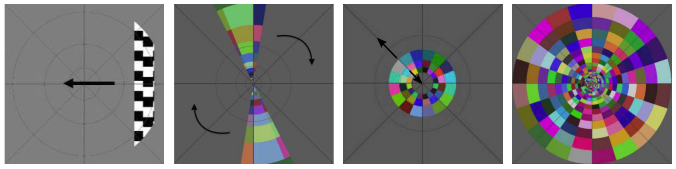

(a) BAR (b) BOWTIE (c) RING (d) FULLFIELD

Figure 5: Examples of visual stimuli presented to the subjects during scanning.

For each subject in the 3T dataset, a T_{1w} image of the entire-brain was acquired using the 3D GRE-MRI sequence, with cubic voxels of 0.75 mm edge length. The T_{1w} image was then upsampled into an image with a resolution of $0.5 \times 0.5 \times 0.5$ mm^3. For each subject in the 7T dataset, a whole-brain anatomical image was collected using an MP2RAGE sequence WIP900b17a (Marques et al., 2010), with a resolution of $0.500 \times 0.533 \times 0.533$ mm^3.

In the first preprocessing step, all fMRI images were motion-corrected using tools in SPM12 (Penny et al., 2006). The 3T dataset was also slice scan time corrected. Hereinafter, the data without motion and slice scan time corrections are referred to as *original* data; and the preprocessed images without SAC are referred to as *uncorrected* data. A T_{1w} alignment image of each subject was

created by aligning the T_{1w} image to an average of two oppositely-distorted images of the subject, through SPM's co-registration procedure (Collignon et al., 1995).

4.2. Performance measures

We quantitatively evaluate the corrected images in three aspects: geometric correction, blurriness, and the suitability for BOLD analysis. The various performance measures are described in this subsection.

Structural similarity measures are used to evaluate how well the corrected fMRI image matches the brain structural given by the T_{1w} image. Here, we used the mutual information (MI) to compute the similarity between the fMRI images and the T_{1w} image (Wells et al., 1996). A smaller value of MI indicates less similarity between the functional and structural T_{1w} images.

The percentage of activated voxel evaluates both the geometric accuracy and the suitability for subsequent BOLD analysis. The reason is that the BOLD response is localized in gray matter and to a certain degree in the cerebrospinal fluid (CSF) more for 3T and less for 7T data, but not in white matter. Distortions of fMRI images result in some significantly modulated voxels being mislocated in white matter of the T_{1w} image. Here, we employ correlation analysis, a common and robust method for analyzing phase-encoded retinotopic mapping data. This analysis provides a phase-map[5] of the BOLD responses (Engel et al., 1997; Schira et al., 2009). Fig. 6 shows an example of a phase-map obtained by correlation analysis of an uncorrected fMRI scan. Voxels with supra-threshold response are marked in color, where the color depicts the phase (delay) of the response, not the strength of the activation. In the given example, there are many activated voxels located in white matter, indicating that they are displaced by distortions.

In this paper, we introduce a measure using the percentage of activated voxels in gray matter and white matter to evaluate the geometric correction in the corrected images. The reasons of measuring the percentage of activated voxels in white matter are: (i) white matter is surrounded by gray matter; (ii) there is a large number of activated voxels aligned to white matter; and (iii) it is easy to obtain an accurate and reliable segmentation of white matter from the T_{1w} image. The percentage of activated voxels in CSF is not considered as it is not diagnostic for geometric accuracy. A higher percentage of activated voxels in gray matter and a lower percentage of activated voxels in white matter indicates a better alignment of the fMRI images to the T_{1w} image.

[5]The term phase-map refers to the use in phase-encoded retinotopic mapping, which is provided by an FFT-based analysis procedure of BOLD time courses. It is different from "phase" in the phase-encoding direction derived from k-space in MRI acquisition.

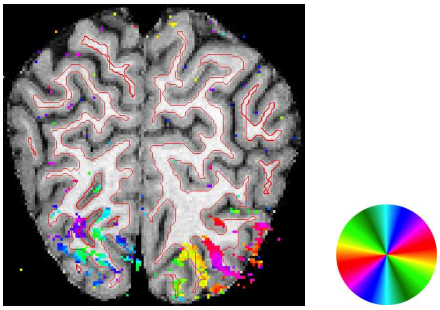

Figure 6: An example of a phase-map in the coronal plane. The red line marks the outer boundary of white matter. Note that the color coding represents the position in the visual field (see the color wheel), not the strength of responses, as typical in phase-encoded retinotopic mapping.

Blurriness measure is used to evaluate how blurry the image is. Introducing blur to high spatial resolution fMRI data is typically undesirable (Polimeni et al., 2018; Huber et al., 2018), as it negates the often considerable effort to achieve high spatial resolution. To measure blurriness, we extended the measure proposed by Crete et al. (2007) for 2D images, to work for 3D images. This measure reflects the intensity variation of an image with respect to that of the low-pass filtered image.

The normalized intensity variation of image I in the i^{th} direction is defined as

$$V_i(I) = \frac{\sum_{\mathbf{p}\in\Omega} \max\{0, \partial_i(I_\mathbf{p}) - \partial_i(I_\mathbf{p} \otimes h_i)\}}{\sum_{\mathbf{p}\in\Omega} \partial_i(I_\mathbf{p})}, \tag{16}$$

where h_i is a low-pass filter, and $\partial_i(I_\mathbf{p})$ is the partial derivative at point $\mathbf{p}$ in the i^{th} direction. The blurriness measure for a 3D image I is the sum of the normalized intensity in three directions

$$M_\mathrm{b}(I) = \frac{1}{3} \sum_{i=1,2,3} [1 - V_i(I)], \tag{17}$$

An image with a higher value of M_b is more blurred than the one with a lower value. Fig. 7 shows an example of the blurriness measure.

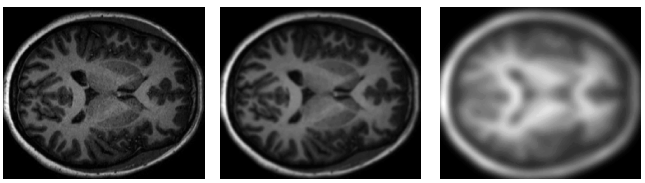

(a) Org., $M_\mathrm{b} = 0.36$ (b) $\sigma = 1$, $M_\mathrm{b} = 0.55$ (c) $\sigma = 5$, $M_\mathrm{b} = 0.71$

Figure 7: Blurriness measurements of an original 3D T_{1w} image and two blurred images, which are produced by two Gaussian smoothing filters with different standard deviations σ.

Suitability for BOLD analysis measures undesired changes in the BOLD responses. For this, we estimate the cumulative distribution function (CDF) of the phase-map

values in every slice. The suitability for BOLD analysis is defined as the difference between the CDFs of corrected and uncorrected data. It is measured by the normalized cross-correlation (NCC) function. The range of NCC is in $[0, 1]$. A small value of NCC indicates a significant change of the BOLD responses between the corrected fMRI images and uncorrected images and vice versa.

4.3. Experimental methods

Scans of inverse blips were first paired together. A mean image over time of each scan was then generated. The mean images of each scan pair were processed by the SAC methods to estimate the displacement field. The estimated displacement field was then used to unwarp all volumes in the scan pair. TISAC and HySCO use the same framework implemented in MATLAB to unwarp the distorted images, while TOPUP uses another framework implemented in C. However, these unwarping frameworks are all based on the cubic spline interpolation.

We evaluated the sub-components of TISAC, which are T_{1w}-based registration (TR), and Bayesian optimization (BO). The tested configurations include: (i) TR only; and (ii) TR with BO (*i.e.* the complete TISAC). For the configuration of TR only, the regularization parameters were selected as $\alpha = 30$, $\beta = 50$, and $\gamma = 75000$.

We further compared the proposed TISAC method with two state-of-the-art SAC methods: HySCO (from the SPM12 toolbox version r7219) and TOPUP (from the FSL package version 5.0.9). For each pair of inverse-PE scans, the displacement field was estimated using two mean images of these scans and then used to unwarp the distorted images from these scans. The regularization parameters of TISAC were selected automatically by applying the BO technique, while these parameters in HySCO were set as $\alpha = 50$ and $\beta = 10$ as suggested in Ruthotto et al. (2012). The regularization parameters of TOPUP were selected as indicated in the preprocessing pipeline for the HCP (Glasser et al., 2013).

We also assessed the time complexity of three SAC methods by recording their execution time with inputs as pairs of mean images. All timing results were collected on a Linux workstation with an Intel Xeon Processor E3-128V2 3.6 GHz and 32 GB RAM.

We evaluated the statistical significance of the measures using two-sample t-tests with the Bonferroni correction. This approach is simple and robust against false positives. The one-way analysis of variance (ANOVA) was used to test the differences in blurriness, MI measure, and percentage of activated voxels among SAC methods. All the tests (two-sample t-tests and ANOVAs) were implemented using MATLAB. The t-test produces a p-value, which is used to evaluate the statistical significance of the test (default significance level is .05). A smaller p-value indicates stronger evidence against the null hypothesis ($\mathcal{H}_0$). A p-value less than .05 means the null hypothesis is rejected at a confidence level of 95%. A p-value greater than 0.05 indicates weak evidence against the null hypothesis.

4.4. Analysis of the proposed method

We investigated whether the BO technique improves the T_{1w}-based registration scheme. Table 3 shows the similarity measures and execution time of the two TISAC settings. It appears that all tested configurations provided corrected images with comparable quality, *i.e.* similarity to the T_{1w} structural image. However, using the BO technique led to a faster run time than when it was not used.

Table 3: Similarity measures and execution times (in seconds) of TISAC configurations: with and without using the BO technique. Methods using BO do not include time for estimating the hyper-parameters.

Measures	TR (mean ± std)	TR + BO (mean ± std)
MIND	0.28 ± 0.02	0.27 ± 0.02
Execution time	25.60 ± 9.33	19.71 ± 8.36

4.5. Comparisons with other SAC methods

First, we investigated the time complexity of the proposed method. Table 4 shows the processing time comparison of three SAC methods: TISAC, TOPUP, and HySCO. The results indicate that the proposed TISAC is significantly faster than TOPUP and HySCO (p-values $< .05$). TISAC is approximate 24.8 times faster than TOPUP, and 1.4 times faster than HySCO.

Table 4: Comparison with other SAC methods in terms of execution time (seconds).

Datasets	TOPUP mean ± std, p-value	HySCO mean ± std, p-value	TISAC mean ± std
3T	399.87 ± 6.52, .000	21.19 ± 5.38, .000	14.88 ± 1.78
7T	741.33 ± 6.04, .000	43.88 ± 12.03, .032	32.58 ± 3.80

The t-test $\mathcal{H}_0$: $t_{\text{TISAC}} \geq t_{\text{other}}$. The p-values are Bonferroni corrected.

Second, we visually assessed the quality of corrected images generated by the three SAC methods. Fig. 8 shows the uncorrected and the corresponding corrected images of these SAC methods for two subjects, one in the 3T dataset (top row) and the other in the 7T dataset (bottom row). The corresponding T_{1w} images are presented in the rightmost column. The figure shows that all tested SAC methods decreased SA distortions noticeably. In both datasets, the TISAC method produced sharp images with clearly visible tissue interfaces, especially near the brain-air interface. In comparison, TOPUP produced low contrast images, and HySCO produced images with artifacts in the brain-air interface (see cyan arrows).

Third, we analyzed the level of blurriness that each SAC method produces. Fig. 9 shows the cumulative distribution of the blurriness measurements of the two datasets for five cases: uncorrected, TOPUP, HySCO, TISAC, and Gaussian filtering of the uncorrected data with a standard deviation of $\sigma = 0.3$. Note that the SA-uncorrected data were obtained by applying the motion correction (MOCO) to the original data. The SAC methods were applied after the MOCO. We observed that the TISAC produced corrected data with the least blur among three SAC methods.

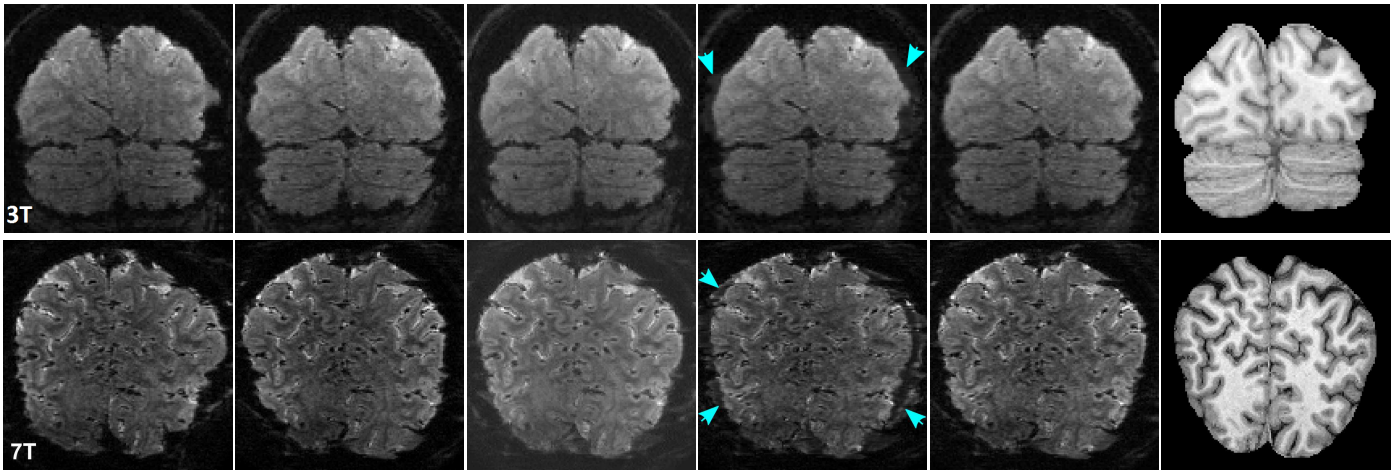

Figure 8: Uncorrected images and their corrected versions created using three SAC methods and corresponding T_{1w} images. *Top row:* images of a subject in the 3T dataset. *Bottom row:* images of a subject in the 7T dataset. The arrows point to the artifacts produced by HySCO.

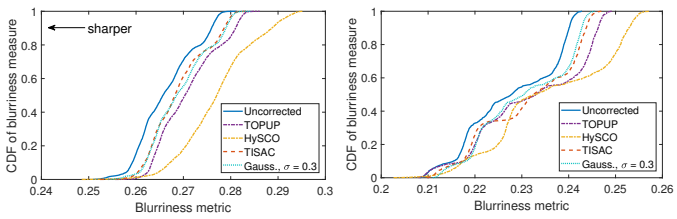

(a) 3T dataset (b) 7T dataset

Figure 9: Cumulative distributions (CDs) of the blurriness measurements of the two datasets for five cases: uncorrected, TOPUP, HySCO, TISAC, and Gaussian filtering of the uncorrected data.

Compared to HySCO, TISAC added significantly less blur on both datasets (p-value = .000, see Table 5). Compared to TOPUP, TISAC added significantly less blur on the 3T dataset (p-value = .000), and slightly less blur on the 7T dataset (p-value = .078). All three SAC methods added blur into the uncorrected data. This observation was confirmed by an one-way ANOVA for each dataset (3T dataset: $F_{3,24956} = 2889.36$, p-value = .000; 7T dataset: $F_{3,6664} = 129.59$, p-value = .000).

Table 5: Comparison with other SAC methods in terms of the blurriness introduced.

Datasets	TOPUP mean ± std, p-value	HySCO mean ± std, p-value	TISAC mean ± std
3T	0.271 ± 0.006, .000	0.277 ± 0.008, .000	0.269 ± 0.006
7T	0.232 ± 0.012, .078	0.236 ± 0.014, .000	0.231 ± 0.011

The t-test $\mathcal{H}_0$: $b_{\text{TISAC}} \geq b_{\text{other}}$. The p-values are Bonferroni corrected.

The proposed TISAC added a similar amount of blur to the MOCO corrected data as did a Gaussian filter with a standard deviation of $\sigma = 0.3$. From a related experiment, we observed that motion correction added a similar amount of blur to the original data as did a Gaussian filter with a standard deviation of $\sigma = 0.35$. Therefore, using the standard deviations of the Gaussian filter as references, we can conclude that TISAC adds less blur to the MOCO corrected images than what motion correction adds to the original images.

Fourth, we computed the structural similarity measures for more quantitative evaluation. Fig. 10 shows box-plots of MI coefficients of the two datasets. For the 3T dataset, the MI coefficients shows a small change between corrected and uncorrected images. An one-way ANOVA showed a significant main effect ($F_{3,49284} = 5.19$, p-value = .001). However, the post-hoc tests revealed that the MI coefficients for TOPUP are significantly larger than all others. The post-hoc tests also showed no difference between the uncorrected, HySCO, and TISAC. For the 7T dataset, all three SAC methods improved the MI coefficients (one-way ANOVA: $F_{3,11397} = 3.08$, p-value = .026), and there was no significance difference between SAC methods (one-way ANOVA: $F_{2,4998} = 1.68$, p-value = .187).

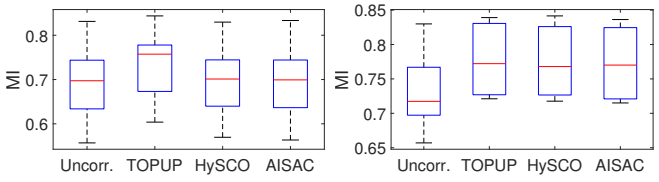

(a) 3T dataset (b) 7T dataset

Figure 10: Box-plots of the MI coefficients between structural T_{1w} and fMRI images.

Fifth, we tested if TISAC improves the accuracy of geometric correction via the BOLD localization in gray matter and white matter. Note that, a high PAV score is desirable in gray matter, whereas a low PAV score is desirable in white matter. Fig. 11 shows phase-maps of uncorrected and three SAC corrected data of a subject in the 7T dataset, with the coronal and axial views. More phase-map examples comparing SAC methods are shown in Figs. A.14 and A.15. Visual inspection reveals that ge-

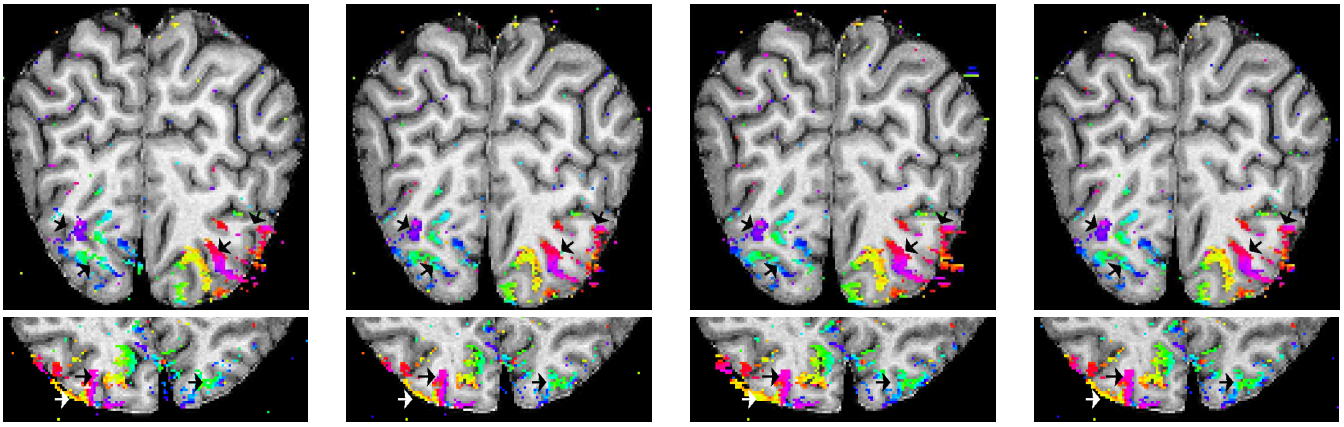

Uncorr. data | TOPUP correction | HySCO correction | TISAC correction

Figure 11: Phase-maps projected onto the T_{1w} image of uncorrected and corrected data in the 7T data of Subject 1. *Top row:* phase-maps in the coronal view. *Bottom row:* phase-maps in the axial view. The arrows point to the areas with large distortions. See the electronic color images.

ometric distortions are smaller in the 3T datasets than in the 7T datasets, where uncorrected 7T data exhibit a clear misalignment between activated voxels and gray matter. The maximum misalignment is 5 pixels (equivalent to about 4.16 mm, see the arrows on the phase-maps of uncorrected data in Fig. 11). Also, visual inspection suggests that TISAC correction produces better alignment than HySCO, and slightly better alignment than TOPUP.

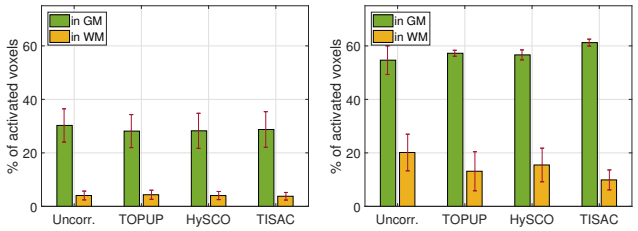

(a) % activated voxels at 3T (b) % activated voxels at 7T

Figure 12: Mean percentage of activated voxels in gray matter and white matter. The error bar shows the corresponding standard deviation of the percentage.

To quantify this, we calculated the percentage of activated voxels (PAV). Fig. 12 shows the PAV measures in gray matter and white matter of the 3T and 7T datasets. For the 3T dataset, the SAC methods did not improve the PAV in gray matter (one-way ANOVA: $F_{2,4998} = 0.84$, p-value $= .473$). They also did not decrease the PAV in white matter (one-way ANOVA: $F_{2,4998} = 0.77$, p-value $= .511$). For the 7T dataset, the PAV measures show a strong improvement for TISAC corrected (see Fig. 12), i.e. the PAV measure in GM of TISAC (mean = 61.22, std = 1.30) is greater than the PAV measure in GM of HySCO (mean = 56.63, std = 1.87), TOPUP (mean = 57.23, std = 1.12), and uncorrected data (mean = 54.66, std = 5.34). However, as there is only a small number of samples, we did not perform a statistical test.

Finally, we evaluated the suitability for BOLD analysis. Table 6 shows the comparison of the normalized cross-correlation between estimated CDFs of the phase values before and after applying SACs. In practice, it is desirable that SAC methods maintain the BOLD responses. The results indicate that the BOLD responses of all three correction methods are not different from those of uncorrected data (one-way ANOVA for 3T dataset: $F_{2,969} = 1.03$, p-value $= .358$; one-way ANOVA for 7T dataset: $F_{2,78} = 0.34$, p-value $= .710$).

Table 6: Change of the BOLD responses after SACs over scans.

Datasets	TOPUP mean ± std, p-value	HySCO mean ± std, p-value	TISAC mean ± std
3T	0.971 ± 0.089, .188	0.964 ± 0.078, .739	0.962 ± 0.089
7T	0.998 ± 0.009, .525	0.999 ± 0.004, .968	0.999 ± 0.004

The t-test $\mathcal{H}_0$: $c_{\text{TISAC}} = c_{\text{other}}$.

4.6. Discussion

The experimental results indicate that SAC methods can correct geometric distortions in EPIs, even when these distortions are severe as in the 7T dataset. HySCO produces corrected images with ghost artifacts around the brain boundary. TOPUP produces images with good distortion corrections and no ghost artifacts, but it introduces blur and affects the BOLD responses. Judged by visual inspection and the performance measures, TISAC produces output images with better alignment to the structural image, compared to TOPUP and HySCO, especially for the dataset with severe geometric distortions.

For high spatial-resolution fMRI, the blurring effects on post-processing are of great concern. We found that all the SAC methods add blur into the corrected images, but the proposed TISAC method adds the least amount. Furthermore, the blur that SAC methods add to the motion-corrected data is much less than the blur that the motion correction step adds to the original data. Evaluation of the structural similarity indicates that the mutual information measure is able to reflect obvious improvements between uncorrected and corrected images.

5. Conclusion

This paper introduced a novel method, called TISAC, for correcting susceptibility artifacts in high spatial resolution EPI-fMRI images. The proposed method uses a pair of inverse-PE EPI-fMRI images and a T_{1w} image. The symmetric registration principle is adopted to combine the inverse-PE images and to produce a corrected image that aligns well with the T_{1w} image. The T_{1w} image is used to regularize the registration, and to select the hyper-parameters via Bayesian optimization.

The performances of TISAC and two other SAC methods were evaluated using two high spatial-resolution EPI-fMRI datasets. The experimental results show that TISAC outperforms the existing methods in terms of accuracy and robustness, particularly in sub-millimeter images obtained by the high field scanner. The proposed method produces sharper corrected images with better geometric correction. It is effective in preserving the structure of the T_{1w} image in regions of significant SA distortions. Furthermore, the proposed method requires less computational resources than TOPUP and HySCO methods. The corrected images produced by TISAC provide better results in subsequent fMRI analysis, while still keeping the BOLD responses as found in the uncorrected images.

Acknowledgment

The authors acknowledge the support of the National Imaging Facility at the Center for Advanced Imaging, University of Queensland. The authors also thank Siemens Healthcare for providing the prototype WIP1080 for data acquisition. This research was supported by two grants (DP140101833 and DP170101778) from the Australian Research Council, and a Matching scholarship from the University of Wollongong.

Declarations of interest

None

Appendix A. Multi-modal similarity measure

Modality independent neighborhood descriptor (MIND) is a multi-dimensional descriptor, which was proposed for computing the dissimilarity measure in multi-modal deformable image registration (Heinrich et al., 2012). This descriptor is independent of the modality, contrast, and noise level of images since it captures the self-similarity of the image patches around a voxel.

The multi-dimensional descriptor s_{MIND} of a voxel $\mathbf{x}$ within the search space $\mathcal{R}$ (centered at $\mathbf{x}$) is a vector with the length as the number of elements in $\mathcal{R}$. The MIND value of a voxel of $\mathbf{x}$ in an image I at a single entry $\mathbf{r}_i \in \mathcal{R}$ is defined as

$$s_{\text{MIND}}(I, \mathbf{x}, \mathbf{r}_i) = \frac{1}{n} \exp\Big(-\frac{d_l(I, \mathbf{x}, \mathbf{r}_i)}{v(I, \mathbf{x})}\Big), \tag{A.1}$$

where n is a constant to normalize the maximum value as 1. Here, $d_l(I, \mathbf{x}_1, \mathbf{x}_2) = \sum_{\mathbf{p}\in\mathcal{P}} G_\sigma(\mathbf{x}_1 + \mathbf{p})(I(\mathbf{x}_1 + \mathbf{p}) - I(\mathbf{x}_2 + \mathbf{p}))^2$ is the patch-based dissimilarity, $\mathcal{P}$ denotes neighborhood indexes of a patch size of $(2l+1)$. The term G_σ denotes the image obtained by applying a Gaussian filter (having the same kernel size as the patch) on the difference image between image I and its shifted version from $\mathbf{x}_1$ to $\mathbf{x}_2$. The term $v(I, \mathbf{x})$ is the mean patch-based dissimilarity of voxel $\mathbf{x}$ in image I with its six neighbors.

The MIND-based dissimilarity of images A and B is defined as the sum of MIND difference at every voxel in the image domain Ω:

$$\mathcal{D}^{\text{MIND}}(A, B) = \frac{1}{|\Omega|} \sum_{\mathbf{x}\in\Omega} \mathcal{D}^{\text{MIND}}(A, B, \mathbf{x}), \tag{A.2}$$

where

$$\mathcal{D}^{\text{MIND}}(A, B, \mathbf{x}) = \frac{1}{|\mathcal{R}|} \sum_{\mathbf{r}_i\in\mathcal{R}} |s_{\text{MIND}}(A, \mathbf{x}, \mathbf{r}_i) - s_{\text{MIND}}(B, \mathbf{x}, \mathbf{r}_i)|. \tag{A.3}$$

A large value of the $\mathcal{D}^{\text{MIND}}$ indicates the more structural dissimilarity between the two images A and B.

Fig. A.13 shows examples of MIND difference maps for different scenarios. The first is the MIND map between T_{1w} images of two different subjects, see Fig. A.13 (d). The second is the MIND map between the T_{1w} image and the EPI image of the same subject, see Fig. A.13 (e). It can be seen that the MIND-based dissimilarity measure between different subjects (T_{1w} to T_{1w}) is larger than the MIND-based dissimilarity measure between different image modalities of the same subject (T_{1w} to EPI).

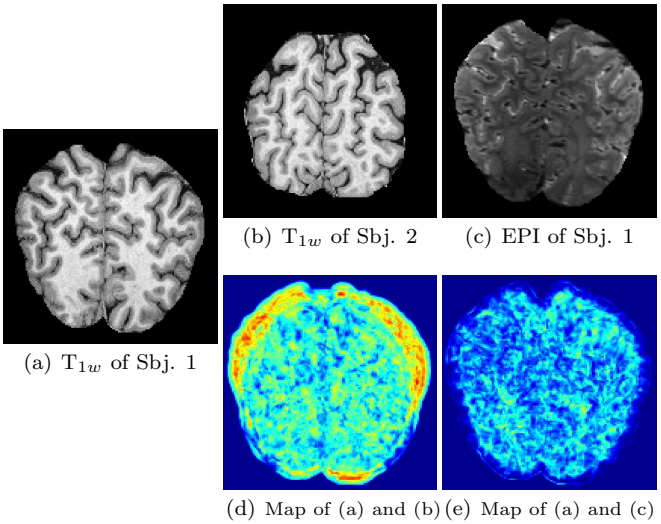

(a) T_{1w} of Sbj. 1 (b) T_{1w} of Sbj. 2 (c) EPI of Sbj. 1 (d) Map of (a) and (b) (e) Map of (a) and (c)

Figure A.13: An example of MIND difference maps between T1w and other MRI types: (a) T_{1w} image of Subject 1; (b) T_{1w} image of Subject 2; (c) EPI image of Subject 1; (d) MIND map of (a) and (b) with MIND score $\mathcal{D} = 0.42$; (e) MIND map of (a) and (c) with MIND score $\mathcal{D} = 0.24$. A blue color denotes a small difference, a red color denotes a large difference. See the electronic color image.

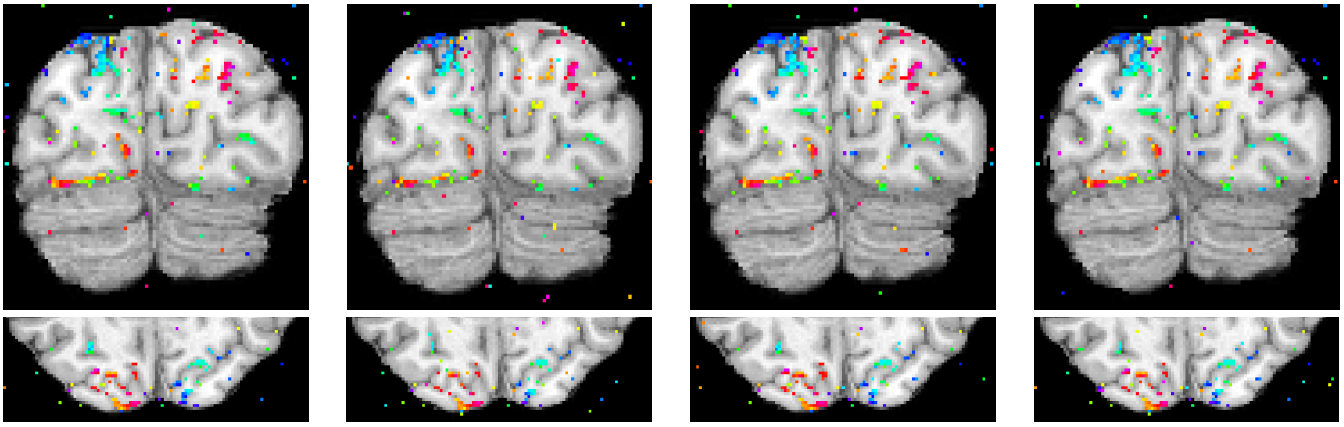

Uncorr. data | TOPUP correction | HySCO correction | TISAC correction

Figure A.14: Phase-maps projected onto the T_{1w} image of uncorrected and corrected data in the 3T data of Subject 2. *Top row:* phase-maps in the coronal view. *Bottom row:* phase-maps in the axial view. See the electronic color images.

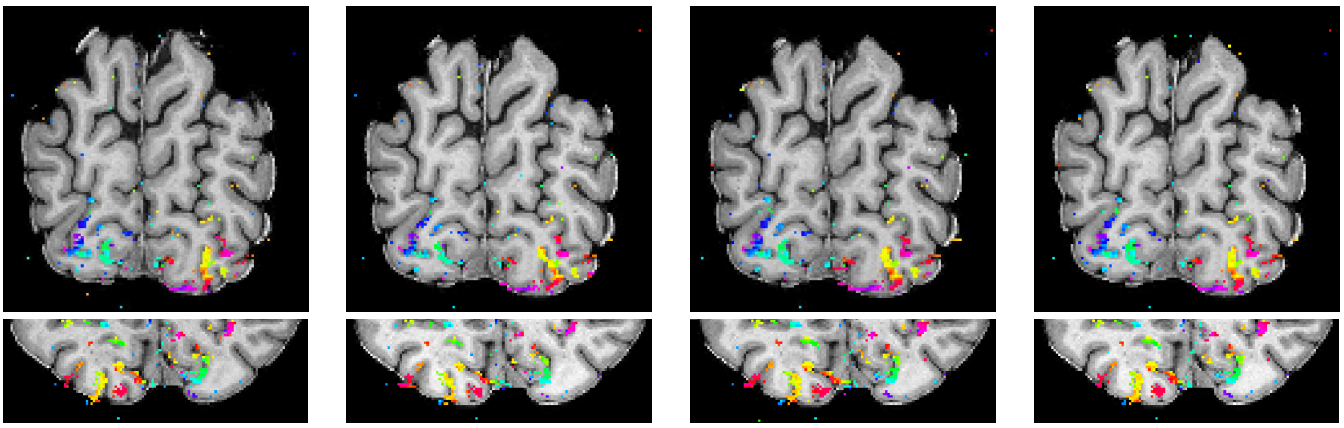

Uncorr. data | TOPUP correction | HySCO correction | TISAC correction

Figure A.15: Phase-maps projected onto the T_{1w} image of uncorrected and corrected data in the 7T data of Subject 3. *Top row:* phase-maps in the coronal view. *Bottom row:* phase-maps in the axial view. See the electronic color images.

Appendix B. Supplementary figures

Figures A.14 and A.15

References

Andersson, J.L.R., Skare, S., Ashburner, J., 2003. How to correct susceptibility distortions in spin-echo echo-planar images: application to diffusion tensor imaging. NeuroImage 20, 870–888. doi:10.1016/S1053-8119(03)00336-7.

Armijo, L., 1966. Minimization of functions having Lipschitz continuous first partial derivatives. Pacific Journal of Mathematics 16, 1–3. doi:10.2140/pjm.1966.16.1.

Bergstra, J., Bardenet, R., Bengio, Y., Kgl, B., 2011. Algorithms for hyper-parameter optimization, in: Proc. Int. Conf. Neural Inf. Process. Sys., pp. 2546–2554.

Bowtell, R., McIntyre, D., Commandre, M., Glover, P., Mansfield, P., 1994. Correction of geometric distortion in echo planar images, in: Proc. Soc. Magn. Reson., p. 411.

Breuer, F.A., Blaimer, M., Mueller, M.F., Seiberlich, N., Heidemann, R.M., Griswold, M.A., Jakob, P.M., 2006. Controlled aliasing in volumetric parallel imaging (2D CAIPIRINHA). Magn. Reson. Med. 55, 549–556. doi:10.1002/mrm.20787.

Brochu, E., Cora, V.M., Freitas, N.d., 2010. A tutorial on Bayesian optimization of expensive cost functions with application to active user modeling and hierarchical reinforcement learning. Computing Research Repository abs/1012.2599.

Burger, M., Modersitzki, J., Ruthotto, L., 2013. A hyper-elastic regularization energy for image registration. SIAM J. Sci. Comput. 35, B 132–148. doi:10.1137/110835955.

Chang, H., Fitzpatrick, J.M., 1992. A technique for accurate magnetic resonance imaging in the presence of field inhomogeneities. IEEE Trans. Imag. Process. 11, 11. doi:10.1109/42.158935.

Chen, N.K., Wyrwicz, A.M., 1999. Correction for EPI distortions using multi-echo gradient-echo imaging. Magn. Reson. Imaging 41, 1206–1213. doi:10.1002/(SICI)1522-2594(199906)41:6<1206::AID-MRM17>3.0.CO;2-L.

Collignon, A., Maes, F., Delaere, D., Vandermeulen, D., Suetens, P., Marchal, G., 1995. Automated multi-modality image registration based on information theory, in: Inf. Process. Med. Imaging, pp. 263–274.

Crete, F., Dolmiere, T., Ladret, P., Nicolas, M., 2007. The blur effect: perception and estimation with a new no-reference perceptual blur metric, in: Proc. Int. Soc. Opt. Engineering, pp. 1–11. doi:10.1117/12.702790.

Engel, S.A., Glover, G.H., Wandell, B.A., 1997. Retinotopic organization in human visual cortex and the spatial precision of functional MRI. Cereb Cortex 7, 181–192. doi:10.1093/cercor/7.2.181.

Essen, D.C.V., Ugurbil, K., Auerbach, E., Barch, D., Behrens, T.E.J., Bucholz, R., Chang, A., Chen, L., Corbetta, M., Curtiss, S.W., Penna, S.D., Feinberg, D., Glasser, M.F., Harel, N., Heath, A.C., Larson-Prior, L., Marcus, D., Michalareas, G., Moeller, S., Oostenveld, R., Petersen, S.E., Prior, F., Schlaggar, B.L., Smith,

S.M., Snyder, A.Z., Xu, J., Yacoub, E., 2012. The human connectome project: a data acquisition perspective. NeuroImage 62, 2222–2231. doi:10.1016/j.neuroimage.2012.02.018.

Glasser, M.F., Sotiropoulos, S.N., Wilson, A.J., Coalson, T.S., Fischl, B., Andersson, J.L., Xu, J., Jbabdi, S., Webster, M., Polimeni, J.R., Essen, D.C.V., Jenkinson, M., 2013. The minimal preprocessing pipelines for the human connectome project. NeuroImage 80, 105–124. doi:10.1016/j.neuroimage.2013.04.127.

Griswold, M.A., Jakob, P.M., Heidemann, R.M., Nittka, M., Jellus, V., Wang, J., Kiefer, B., Haase, A., 2002. Generalized autocalibrating partially parallel acquisitions (GRAPPA). Magn. Reson. Med. 47, 1202–1210. doi:10.1002/mrm.10171.

Haber, E., Modersitzki, J., 2007. Intensity gradient based registration and fusion of multi-modal images. Methods Inf. Med. 46, 292–299. doi:10.1160/ME9046.

Heinrich, M.P., Jenkinson, M., Bhushan, M., Matin, T., Gleeson, F.V., Brady, S.M., Schnabel, J.A., 2012. MIND: Modality independent neighborhood descriptor for multi-modal deformable registration. Med. Image. Anal. 16, 1423–1435. doi:10.1016/j.media.2012.05.008.

Holland, D., Kuperman, J.M., Dale, A.M., 2010. Efficient correction of inhomogeneous static magnetic field-induced distortion in echo planar imaging. NeuroImage 50, 175–184. doi:10.1016/j.neuroimage.2009.11.044.

Hong, X., To, X.V., Teh, I., Soh, J.R., Chuang, K.H., 2015. Evaluation of EPI distortion correction methods for quantitative MRI of the brain at high magnetic field. Magn. Reson. Imaging 33, 1098–1105. doi:10.1016/j.mri.2015.06.010.

Howarth, C., Hutton, C., Deichmann, R., 2006. Improvement of the image quality of T1-weighted anatomical brain scans. NeuroImage 29, 930–937. doi:10.1016/j.neuroimage.2005.08.004.

Huber, L., Ivanov, D., Handwerker, D.A., Marrett, S., Guidi, M., Uluda, K., Bandettini, P.A., Poser, B.A., 2018. Techniques for blood volume fMRI with VASO: From low-resolution mapping towards sub-millimeter layer-dependent applications. NeuroImage 164, 131–143. doi:10.1016/j.neuroimage.2016.11.039.

Hutton, C., Bork, A., Josephs, O., Deichmann, R., Ashburner, J., Turner, R., 2002. Image distortion correction in fMRI: a quantitative evaluation. NeuroImage 16, 217–240. doi:10.1006/nimg.2001.1054.

Irfanoglu, M.O., Modia, P., Nayaka, A., Hutchinson, E.B., Sarllsc, J., Pierpaoli, C., 2015. DR-BUDDI (Diffeomorphic Registration for Blip-Up blip-Down Diffusion Imaging) method for correcting echo planar imaging distortions. NeuroImage 106, 284–299. doi:10.1016/j.neuroimage.2014.11.042.

Jezzard, P., Balaban, R.S., 1995. Correction for geometric distortion in echo planar images from B0 field variations. Magn. Reson. Med. 34, 65–73. doi:10.1002/mrm.1910340111.

Kadah, Y.M., Hu, X., 1997. Simulated phase evolution rewinding (SPHERE): a technique for reducing B0 inhomogeneity effects in MR images. Magn. Reson. Med. 38, 615–627. doi:10.1002/mrm.1910380416.

Kybic, J., Thevenaz, P., Nirkko, A., Unser, M., 2000. Unwarping of unidirectionally distorted EPI images. IEEE Trans. Med. Imag. 19, 80–93. doi:10.1109/42.836368.

Ludeke, K.M., Roschmann, P., Tischler, R., 1985. Susceptibility artifacts in NMR imaging. Magn. Reson. Imaging 3, 329–343. doi:10.1016/0730-725X(85)90397-2.

Marques, J.P., Kober, T., Krueger, G., Zwaag, W.V.d., Moortele, P.F.V.d., Gruetter, R., 2010. MP2RAGE, a self bias-field corrected sequence for improved segmentation and T1-mapping at high field. NeuroImage 49, 1271–1281. doi:10.1016/j.neuroimage.2009.10.002.

McRobbie, D.W., Moore, E.A., Graves, M.J., Prince, M.R., 2003. MRI from Picture to Proton. Cambridge University Press.

Mugler III, J.P., Brookeman, J.R., 1990. Three-dimensional magnetization-prepared rapid gradient-echo imaging (3D MP RAGE). Magn. Reson. Med. 15, 152–157. doi:10.1002/mrm.1910150117.

Munger, P., Crelier, G.R., Peters, T.M., Pike, G.B., 2000. An inverse problem approach to the correction of distortion in EPI images. IEEE Trans. Med. Imag. 19, 681–689. doi:10.1109/42.875186.

Nocedal, J., Wright, S.J., 1999. Numerical Optimization. Springer, New York. doi:10.1007/b98874.

Ogawa, S., Lee, T.M., Kay, A.R., Tank, D.W., 1990. Brain magnetic resonance imaging with contrast dependent on blood oxygenation, in: National Academy of Sciences of the United States of America, pp. 9868–9872. doi:10.1073/pnas.87.24.9868.

Penny, W., Friston, K., Ashburner, J., Kiebel, S., Nichols, T., 2006. Statistical Parametric Mapping: The Analysis of Functional Brain. 1 ed., Academic Press.

Polimeni, J.R., Renvall, V., Zaretskaya, N., Fischl, B., 2018. Analysis strategies for high-resolution UHF-fMRI data. NeuroImage 168, 296–320. doi:10.1016/j.neuroimage.2017.04.053.

Poser, B.A., Ivanov, D., Kemper, V.G., Kannengiesser, S.A., Uludag, K., Barth, M., 2013. CAIPIRINHA-accelerated 3D EPI for high temporal and/or spatial resolution EPI acquisitions, in: Proc. European Soc. Magn. Reson. Med. Biol. Meeting, pp. 226–226.

Poser, B.A., Koopmans, P.J., Witzel, T., Wald, L.L., Barth, M., 2010. Three dimensional echo-planar imaging at 7 Tesla. NeuroImage 51, 261–266. doi:10.1016/j.neuroimage.2010.01.108.

Reber, P.J., Wong, E.C., Buxton, R.B., Frank, L.R., 1998. Correction of off resonance related distortion in echo-planar imaging using EPI-based field maps. Magn. Reson. Med. 39, 328–330. doi:10.1002/mrm.1910390223.

Robson, M.D., Gore, J.C., Constable, R.T., 1997. Measurement of the point spread function in MRI using constant time imaging. Magn. Reson. Med. 38, 733–740. doi:10.1002/mrm.1910380509.

Ruthotto, L., Kugel, H., Olesch, J., Fischer, B., Modersitzki, J., Burger, M., Wolters, C.H., 2012. Diffeomorphic susceptibility artifact correction of diffusion-weighted magnetic resonance images. Phys. Med. Biol. 57, 5715–5731. doi:10.1088/0031-9155/57/18/5715.

Ruthotto, L., Mohammadi, S., Heck, C., Modersitzki, J., Wiskopf, N., 2013. Hyper-elastic susceptibility artifact correction of DTI in SPM. Springer Berlin Heidelberg. book section 60. pp. 344–349. doi:10.1007/978-3-642-36480-8_60.

Schira, M.M., Tyler, C.W., Breakspear, M., Spehar, B., 2009. The foveal confluence in human visual cortex. Journal of Neuroscience 29, 9050–9058. doi:10.1523/jneurosci.1760-09.2009.

Schmitt, F., 2015. Echo-Planar Imaging. Academic Press. volume 1. book section 6. pp. 53–74.

Setsompop, K., Gagoski, B.A., Polimeni, J.R., Witzel, T., Wedeen, V.J., Wald, L.L., 2011. Blipped-controlled aliasing in parallel imaging for simultaneous multislice echo planar imaging with reduced g-factor penalty. Magn. Reson. Med. 67, 1210–1224. doi:10.1002/mrm.23097.

Snoek, J., Larochelle, H., Adams, R.P., 2012. Practical Bayesian optimization of machine learning algorithms, in: Proc. Int. Conf. Neural Inf. Process. Sys., pp. 2951–2959.

Studholme, C., Constable, R.T., Duncan, J.S., 2000. Accurate alignment of functional EPI data to anatomical MRI using a physics-based distortion model. IEEE Trans. Med. Imag. 19, 1115–1127. doi:10.1109/42.896788.

Techavipoo, U., Lackey, J., Shi, J., Leist, T., Lai, S., 2008. Geometric distortion correction in EPI by phase labeling using sensitivity encoding (PLUS), in: Proc. IEEE Intern. Symp. on Biomed. Imaging, pp. 556–559. doi:10.1109/ISBI.2008.4541056.

Wan, X., Gullberg, G.T., Parker, D.L., Zeng, G.L., 1997. Reduction of geometric and intensity distortions in echo planar imaging using a multi-reference scan. Magn. Reson. Med. 37, 932–942. doi:10.1002/mrm.1910370619.

Wells, W.M., Viola, P., Atsumi, H., Nakajima, S., Kikinis, R., 1996. Multi-modal volume registration by maximization of mutual information. Med. Image. Anal. 1, 35–51. doi:10.1016/S1361-8415(01)80004-9.

Wu, D.H., Guo, Y., Lu, C.C., Suri, J., 2006. Improvement to functional magnetic resonance imaging (fMRI) methods using non-rigid body image registration methods for correction in the presence of susceptibility artifact effects, in: Proc. Inter. Conf. IEEE Eng. Med. Biol. Soc., pp. 1018–1020. doi:10.1109/IEMBS.2006.259943.

Wu, M., Chang, L.C., Walker, L., Lemaitre, H., Barnett, A.S., Marenco, S., Pierpaoli, C., 2008. Comparison of EPI distortion correction methods in diffusion tensor MRI using a novel framework. Med. Image. Comput. Assist. Interv., Springer Berlin Heidelberg.

Zaitsev, M., Hennig, J., Speck, O., 2004. Point spread function mapping with parallel imaging techniques and high acceleration factors: fast, robust, and flexible method for echo planar imaging distortion correction. Magn. Reson. Med. 52, 1156–1166. doi:10.1002/mrm.20261.

Zeng, H., Constable, R.T., 2002. Image distortion correction in EPI: comparison of field mapping with point spread function mapping. Magn. Reson. Med. 48, 137–146. doi:10.1002/mrm.10200.